The Thesis Committee for Samantha Sparr Taylor
Certifies that this is the approved version of the following thesis:

Thermal History Correlation with Mechanical Properties for Polymer Selective Laser Sintering (SLS)

APPROVED BY
SUPERVISING COMMITTEE:

Supervisor:

Joseph J. Beaman, Jr.

Scott Fish

Thermal History Correlation with Mechanical Properties for Polymer Selective Laser Sintering (SLS)

by

Samantha Sparr Taylor, B.S.M.E.

Thesis

Presented to the Faculty of the Graduate School of

The University of Texas at Austin

in Partial Fulfillment

of the Requirements

for the Degree of

Master of Science in Engineering

The University of Texas at Austin

May 2017

Acknowledgements

I would like to thank my advisors Dr. Beaman and Dr. Fish for giving me the opportunity to work with them. They have been endless sources of inspiration and knowledge, without which none of this would have been possible. They have given me the freedom to explore my research interests, while still guiding me through my academic endeavors.

I would like to thank all my lab mates and colleagues who made this work possible. In particular, Tim Phillips, Austin McElroy, Jimmy Ji, and Adam Lewis. Their support and countless hours spent building and running tests on our machine have brought us to where we are today.

Lastly, I would like to thank my parents for their continual support and guidance. I am so grateful for the gifts and opportunities they have given me. I would like to thank them for all the advice and patience they have given me throughout my career.

Abstract

Thermal History Correlation with Mechanical Properties for Polymer Selective Laser Sintering (SLS)

Samantha Sparr Taylor, M.S.E.

The University of Texas at Austin, 2017

Supervisor: Joseph J. Beaman, Jr.

This thesis investigates the in-situ thermal history of parts manufactured with the Selective Laser Sintering (SLS) process. It compares the effectiveness of two different cameras, a stationary reference mid-wave infrared (IR) and a bore-sighted mid-wave IR camera, by evaluating correlations between strength, elongation, and fracture location to the observed thermal history of the selective laser sintered parts produced. ZYX tensile bars were built to leverage the high dependence of tensile strength on interlayer bonding, which is generally assumed to be related to thermal conditions from layer to layer. Various thermal history analysis methods, for example: cold subregion temperature, average layer temperature, and outline average temperature, were examined to discover the best method for predicting fracture location and correlating with build strength. In addition, several smoothing techniques that reduced the noise over time when using the different thermal analysis methods were assessed in their ability to improve the correlation of the given thermal method to the mechanical strength and fracture location.

Table of Contents

List of Tables

List of Figures

Chapter 1: Background

Process monitoring is always key for any manufacturing procedure to ensure the quality of the resultant parts. For additive manufacturing, process monitoring is paramount since within the process, not only are the dimensions of the part being formed but so are its material properties. Virtually all additive manufacturing processes are layerwise processes. Specifically, in the selective laser sintering (SLS) process parts are formed by layers, about 100 microns thick, of powder being sintered together to form a 3D part. An image of this process can be found below in Figure 1.

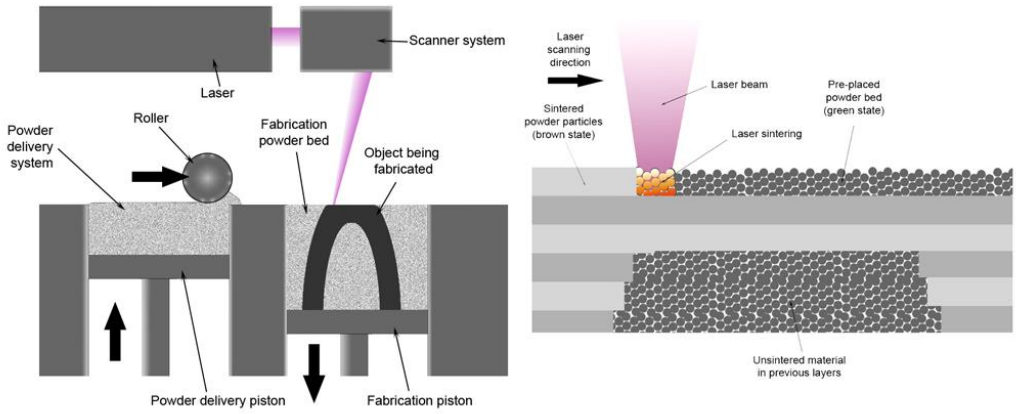

Figure 1: Selective Laser Sintering Process Diagram (SPI Lasers Limited, 2015)

The selective laser sintering process was developed at the University of Texas at Austin in the 1980's (Austin, 2012). For polymers, the key to the process is to hold the temperature of the powder bed that is being sintered to create the part above the glass transition temperature of the material. This prevents the polymer from re-crystalizing and allowing successive layers to be properly bonded together. This elevated temperature also diminishes the required laser power to

cause full melting. The thermal state of the powder bed is key in developing desired material properties.

As with all additive manufacturing processes, the layerwise creation of the part can produce anisotropic part properties. In the SLS process, the strength of a part perpendicular to the layer stratification is often weakest because of the interlayer bonds (Bourell, Watt, Leigh, & Fulcher, 2014). In this experiment, the parts will be built with the longest dimension of the specimen being along the Z axis which is perpendicular to the layer stratification in order to focus on the strength of the interlayer bonds. The strength of the interlayer bonds is strongly dependent on the thermal state of the layer as mentioned in Bourell et. al (Bourell, Watt, Leigh, & Fulcher, 2014).

For monitoring the thermal state of a build, the most common method in commercial SLS machines is a single point measurement of the entire build surface. This single point measurement is then mapped to correspond to specific regions of the build surface in order to control the multiple radiation based heaters that perform the finer thermal control of the build surface. In literature, the most common method for monitoring the thermal state of a build in a lab setting is infrared (IR) thermography. Most work has been done with thermal monitoring of the Direct Metal Laser Sintering (DMLS) process. As seen in Krauss et. al., an IR camera was mounted outside the machine to monitor the temperature of each layer to check the quality of the build (Krauss, Eschey, & Zaeh, 2012). Others have directly monitored the thermal state of the melt pool using various sensors such as a pyrometer and pieced the data together to get an overall image of a part for each layer as seen in Buls et. al. (Buls, Clijsters, & Kruth, 2014). For this experiment, two IR cameras were used to monitor the build process and will be described further in the experimental setup. A specialized research machine, which is unique to University of Texas at Austin (UT Austin) and

will be described in greater detail in the following section, was used to enable the two camera protocol.

Similar work to this experiment has been performed previously by using only one long-wave infrared camera on the same machine (Wroe, Improvements and Effects of Thermal History on Mechanical Properties for Polymer Selective Laser Sintering (SLS), 2015). This thesis' experiment used two different mid-wave infrared (MWIR) cameras. The mid-wave cameras do not risk being damaged or influenced by the CO_2 laser wavelength of 10.6 microns due to the cameras only measuring in the 3-5 micron range (FLIR, 2017), whereas the long-wave infrared camera measures in the 7.5-13 micron range (FLIR, 2017). One major benefit of the MWIR cameras is that they can achieve faster frame rates which is employed in this experiment with the bore-sighted camera. Another benefit the MWIR cameras is that they can have better temperature sensitivity (Optotherm Thermal Imaging, 2017). This is key in discovering small temperature gradients, which will be necessary for the focus of the data analysis.

Chapter 2: Experimental Setup

The SLS builds for this experiment were conducted using the Laser Additive Manufacturing Pilot System (LAMPS). This system is unique to the University of Texas at Austin and will be discussed in this section. More in depth descriptions of all aspects of the machine can be found in Wroe et. al. (Wroe, Improvements and effects of thermal history on mechanical properties for polymer selective laser sintering (SLS), 2015). Descriptions of the builds and how they were conducted is also included in this section.

LAMPS Machine

The Laser Additive Manufacturing Pilot System (LAMPS) is a custom built research SLS machine that enables the monitoring and control of virtually every process parameter during a build process. For monitoring, the machine has over 40 thermocouples, a Edmund Optic Monochrome USB camera (visual camera) with a frame rate of 25 Hz (Edmund Optics Inc., 2017), a FLIR 6701 MWIR camera with a stationary reference frame (stationary reference camera) and a frame rate of 30 Hz (FLIR, 2017), and a bore-sighted FLIR SC8243 MWIR camera (bore-sighted camera) with a frame rate of 2.24 kHz (FLIR Systems, Inc., 2013). A visual representation of this machine can be found in Figure 2.

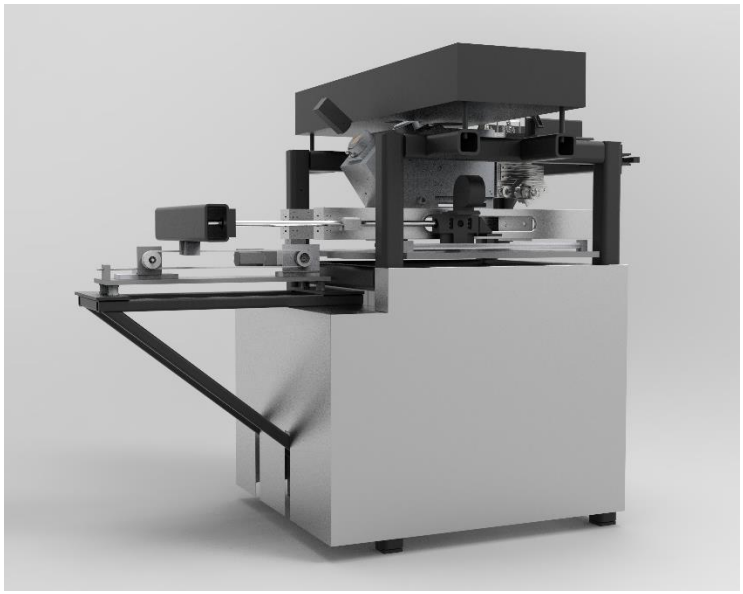

Figure 2: LAMPS Machine

All of the thermocouples and the stationary reference camera are used in the control of the machine's various heaters and quartz lamps in addition to the monitoring of the build process. The quartz lamps provide higher accuracy temperature control of the powder bed keeping the powder bed above its glass transition temperature as is the practice in the SLS process. The visual and bore-sighted cameras are used solely for monitoring purposes at the moment. The location of the stationary reference and bore-sighted cameras are outlined in red in Figure 3 below.

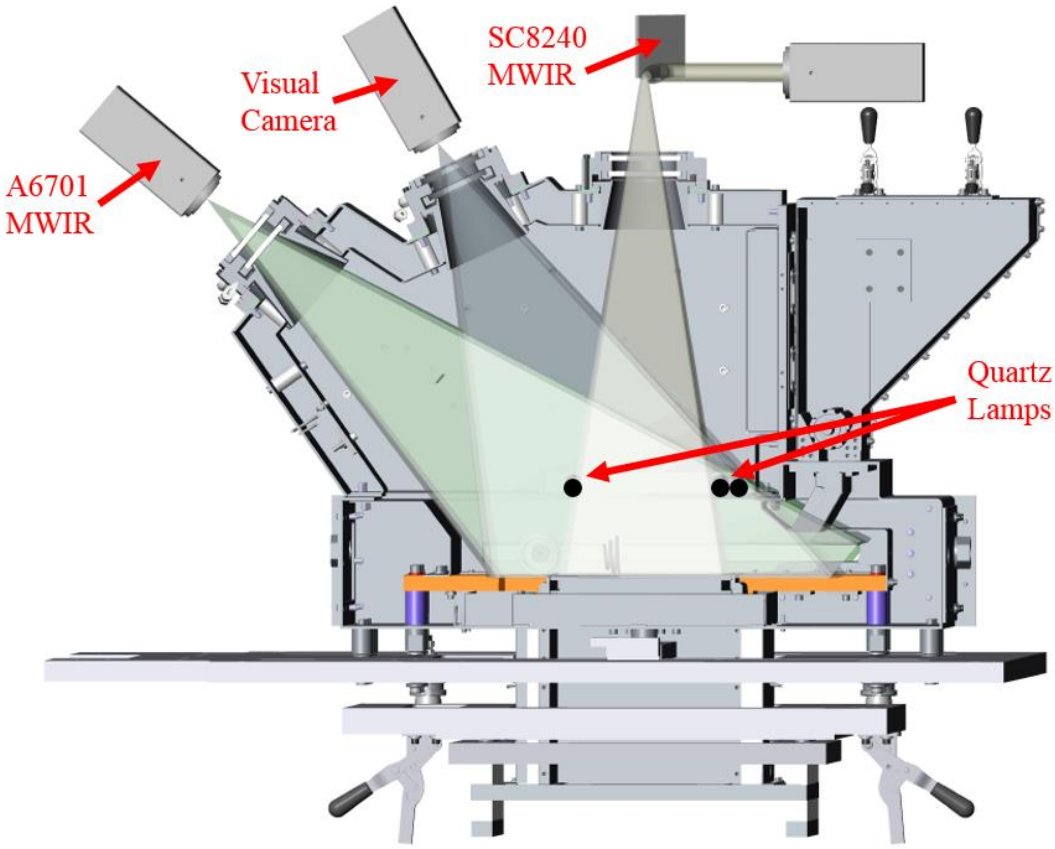

Figure 3: LAMPS Cross Section View; All cameras with field of views highlighted.

The LAMPS machine employs the use of a dichroic mirror placed in the optical track of the laser in order to bore-sight the 2.24 kHz FLIR SC8243 MWIR camera with the laser. The dichroic mirror allows for both the laser and the SC8243 MWIR's camera field of view to both travel through the galvanometers, allowing for the camera's images to always be aligned about the moving laser spot. In Figure 4, all the optical track components described are identified.

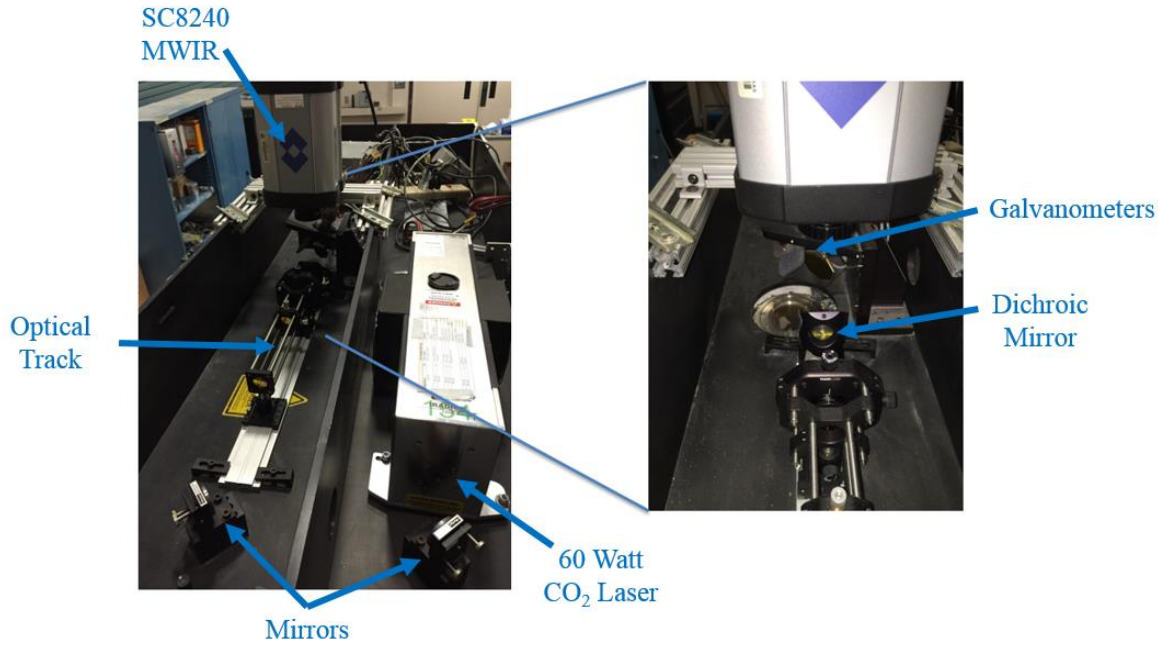

Figure 4: LAMPS Optical Track with highlighted components

Build Setup

Two builds were conducted for this experiment. Each build consisted of 30 tensile bars arranged in a 3 row, 10 column array with the longest dimension of the bars along the Z axis, as seen in Figure 5.

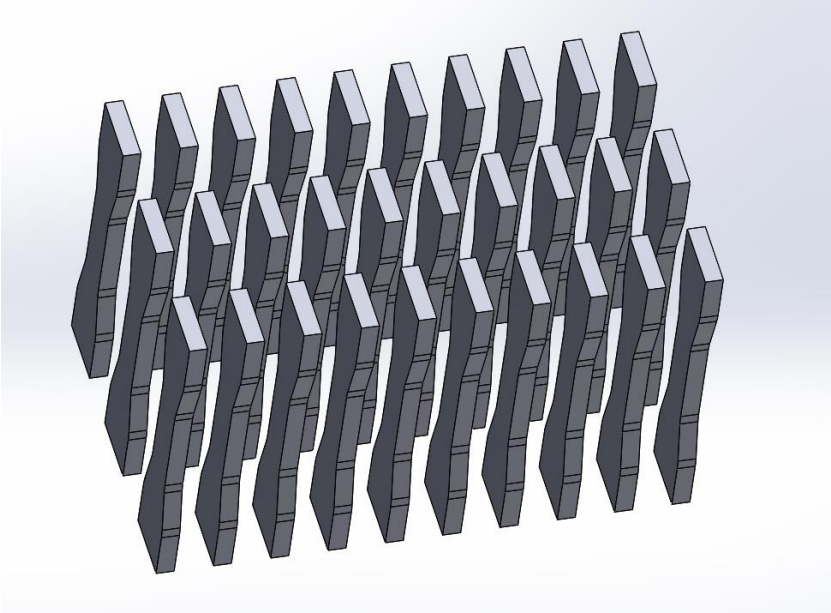

Figure 5: 30 ZYX Tensile Bar Isometric View.

The tensile bar specimens were similar to ASTM Type A but with a length of 72 mm, a gage section length of 21 mm, and a thickness of 4 mm. The dimensions in millimeters can be seen in Figure 6.

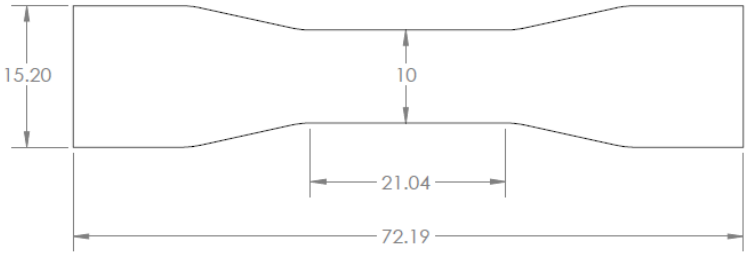

Figure 6: Tensile Bar Dimensions in Millimeters.

The builds were positioned towards one side of the build chamber to prevent the quartz lamp from obscuring the field of view of the stationary reference camera. An image from this camera can be seen in Figure 7.

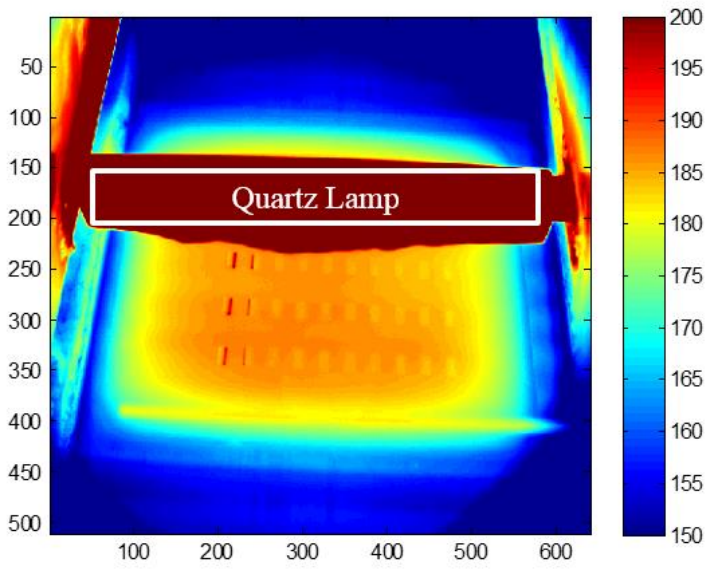

Figure 7: Stationary Reference Camera View of Build Chamber

The quartz lamp with its heat shield atop it can be seen crossing above the tensile bar array in the middle of the image. The heat shield prevents the quartz lamp's radiation from saturating the camera's sensor. Care was taken to ensure the heat shield did not block part of the build surface from the camera's view. Therefore, the part locations were in the forward half of the build area to allow for the camera to view all parts in the build. In regards to the bore-sighted camera, the laser has full view of the build surface therefore there is no visual interference with the heat shield and the bore-sighted camera.

Both builds were conducted with the same lot of Nylon 12 PA 650 powder from Advanced Laser Materials (ALM). All machine parameters were held constant between the builds, except for the set point for the quartz lamps that control the build surface temperature was raised one degree for the second build due to curling issues seen in the beginning of the build. For both builds, the two MWIR cameras' images were recorded throughout the entire gage section of the tensile specimens. The stationary reference camera's images are 512x640 pixels and are taken at a frame rate of 30 Hz. The bore-sighted camera's images are 64x64 pixels and are taken at a frame rate of

2.2 kHz. An example of each camera's image can be seen in Figure 8. The bore-sighted image, seen in Figure 8, has two tensile bar cross sections in its field of view. The laser spot location in the image is indicated while it is in the middle of sintering a single scan line.

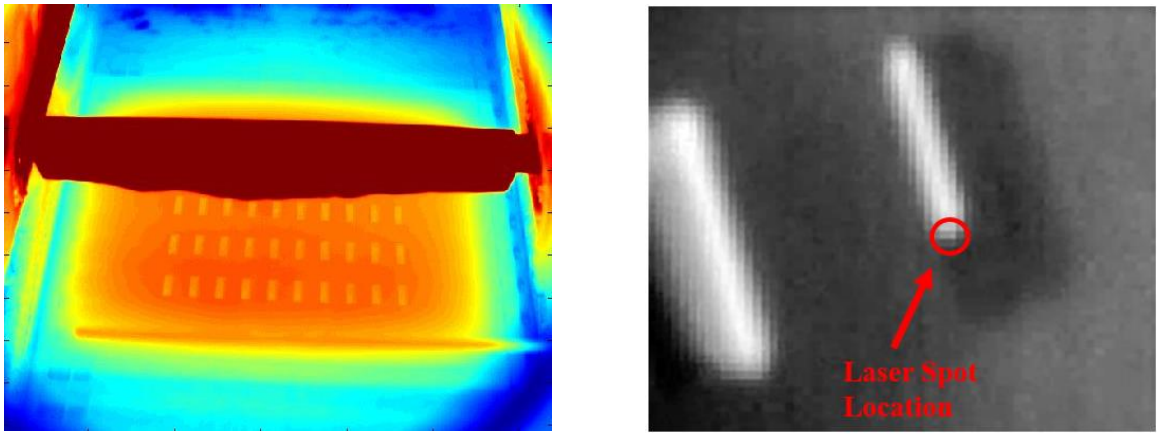

Figure 8: (LEFT) Image taken from Stationary Reference MWIR Camera (RIGHT) Image Taken from Bore-sighted MWIR Camera.

The scan strategy employed for both builds was completing all the fill scans for all parts and then perform all the outline scans for each part. The fill scan strategy alternated between layers. For the even layers, all fill scan lines were parallel to the Y axis, or vertical as viewed in the left side of Figure 9. The odd layers had fill scan lines parallel to the X axis, or horizontal as viewed in the right side of Figure 9. The scan line continues along a single coordinate for all bars along that coordinate. Therefore, for the even layers, each column was sintered at the same time, and for the odd layers, each row was sintered at the same time. This strategy helps reduce the time for scanning as the laser's position does not change directions as frequently, which lengthens the sintering process, as compared to other scanning strategies. This scan strategy was implemented in the LAMPS machine as it is a common practice in commercial manufacturers.

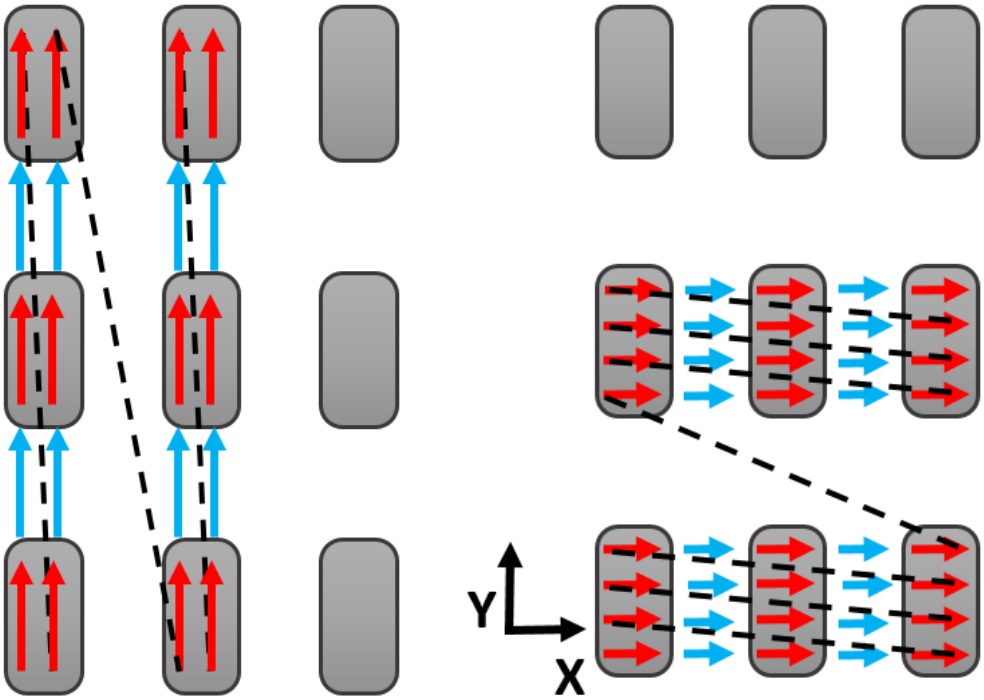

Figure 9: (LEFT) Y axis or Vertical Scan Line Strategy (RIGHT) X Axis or Horizontal Scan Line Strategy.

Tensile Test Methodology

Once each build was completed, the specimens were tensile tested according to ASTM 638 methodology with an Instron 3345 testing machine. The stress-strain plot was found for each tensile bar tested. From that plot, the ultimate tensile strength, which was taken as the maximum stress seen during the test, and elongation at break, which was the value of strain at the time of fracture, were found for each tensile bar. To determine exactly where the break of the tensile bar occurred, the total length of the bar was measured before testing and the resultant two parts of the broken bar were measured after tensile testing. Images of before and after a single tensile bar was tested can be seen below in Figure 10.

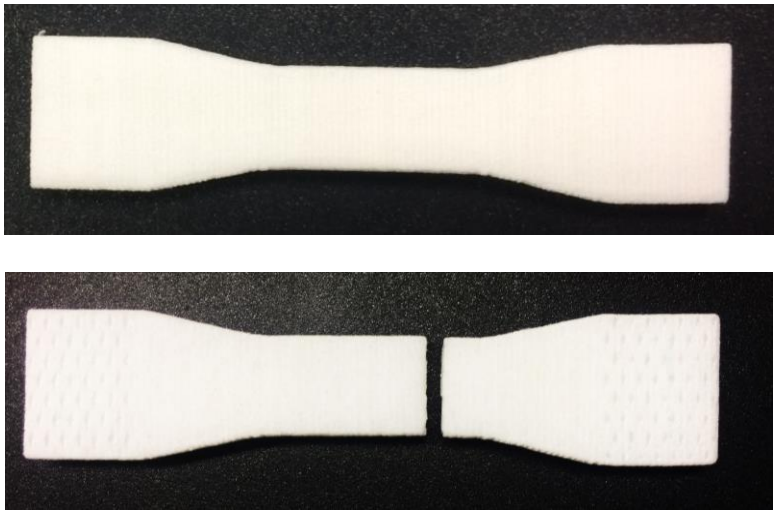

Figure 10: (TOP) Tensile Bar before Testing (BOTTOM) Fractured Tensile Bar.

The lengths of each half were converted to a layer number using the average layer thickness which was around 3.9 thousandths of an inch. Due to the slight plastic deformation seen by the bars and the fact that not all fracture surfaces occurred within a single layer, there is a range of uncertainty for the exact fracture layer. This error bar range was calculated using the phenomena above, which totaled to +/- 30 layers.

Chapter 3: Post-Build Analysis

The images collected during both builds from the stationary reference camera and bore-sighted camera totaled over 1.5 TB of data. This data however was reduced through analysis to filter the data down to about 1 GB of data that was used in the final thermal correlations. For the filtering process, different schemes were used for each camera's images in order to select the final data for each tensile bar. The main goal of this initial data analysis was to pick out from the images of each camera a pre-sintered image of each bar and a post-sintered image of each bar. The post-sintered image of each bar for each layer will reveal the quality of the sintered layer through its thermal state. This image will reveal any gradients caused by the laser and initial powder bed. The reason a pre-sintered image is important is that it has been shown in Philips et. al. that the thermal gradients present in the powder surface pre-sintering are also present post-sintering just at an elevated temperature due to the laser's energy input (Phillips, McElroy, Fish, & Beaman, 2016). Therefore, the post-sintered image and pre-sintered images should be nearly identical except for a temperature shift. The pre-sintered image is key especially with regards to the stationary reference camera with its 30 Hz frame rate.

Due to the changing emissivity of the powder once it is in its melted state, when imaged, the tensile bars appear colder than the real temperature when the image is taken due to the time lapse of when the post-sintered image is taken and the beginning of the bar was scanned as seen in Figure 11. Figure 11 is a single tensile bar which has been lased using the X-direction scan strategy as seen in Figure 9 with scan lines being vertical and successive passes moving from left to right. The left side of the tensile bar in Figure 11 appears to indicate that it is cooler than the right side and the surrounding powder bed. This is being caused by the changing emissivity when

the part is melted then re-solidified. The emissivity of the powder is different from the emissivity of the melt pools as well as the solidified part. The camera's emissivity is set for the powder because the camera is controlling the quartz lamps that heat the powder bed to keep it above its glass transition temperature and be hot enough to prevent curling of parts when lasing occurs. Therefore, the pre-sintered image removes most emissivity differences out of consideration.

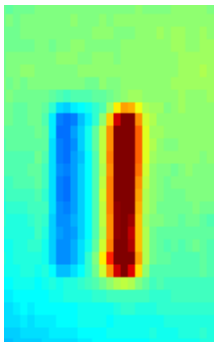

Figure 11: Stationary Reference Camera Post-Sintered Image Zoomed in to One Tensile Bar.

Stationary Reference 6701 MWIR Camera Analysis

The stationary reference camera's field of view is of the entire lower half of the chamber of LAMPS machine as can be seen in Figure 7. The camera's image is 512x640 pixels with each pixel's resolution being roughly 300 microns laterally and 650 microns vertically. This camera's primary use is controlling the three quartz lamps that provide the finer temperature control on the build surface. The camera's field of view is sufficient to include both the powder bed and the powder drop area as shown in Figure 12. One quartz lamp is dedicated to the powder drop area where the powder dropped from the feed hopper into the chamber is flash heated before it is spread by the roller. These areas are blocked out in Figure 12. The other two quartz lamps are at either side of the powder surface, each one heating half of the powder bed. The quartz lamp as mentioned previously provide the higher accuracy thermal control of the powder bed.

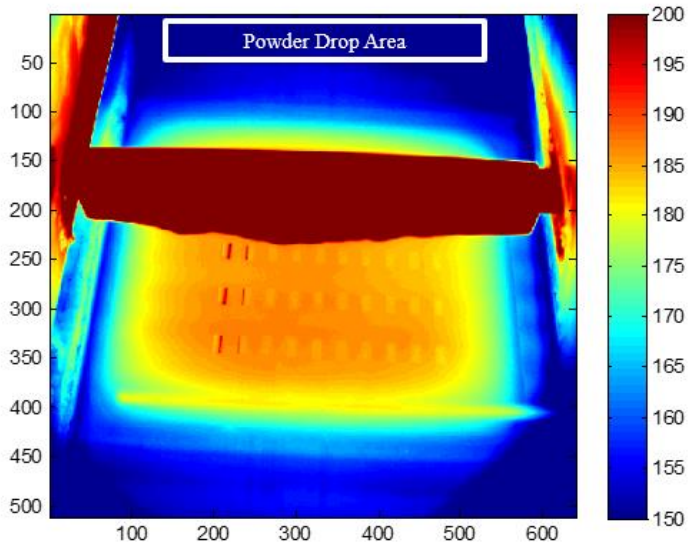

Figure 12: Original Image from Stationary Reference Camera.

The first step in picking out the pre- and post-sintered images for the stationary reference camera is to perform a 2D spatial transformation of the images to make all the cross section of the bars rectangular in shape to allow for a consistent spatial analysis for the entire build. This corrects for the camera's angle which is about 45 degrees from the normal of the build surface. The spatial transformation allows the rectangular cross section of the tensile bars to correlate with a set of identically sized matrices of pixels in the resultant image. This aids the analysis process immensely as thermal analysis models that rely on a certain fraction of pixels that are equal in the transformed space for all bars, regardless of their location in the original image. An image of the build area before and after the transformation can be found in Figure 13.

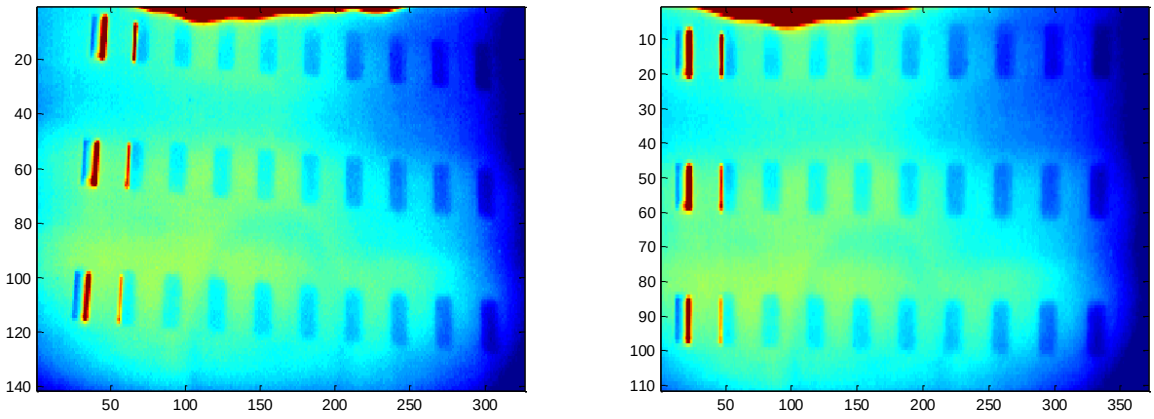

Figure 13: (LEFT) Stationary Reference Camera Raw Image of Build Area Before the Transformation (RIGHT) Stationary Reference Camera Processed Image of Build Area after the Transformation.

Both the pre- and post-sintered images come from single frames from the stationary reference camera due to aliasing caused from the laser's speed of 1.5 m/s being significantly faster than the camera's frame rate of 30 Hz. If several images were gathered and combined to form, for example, the post-sintered image, the number of frames used and the location where sintering occurred would not be consistent from layer to layer or even bar to bar within a single layer. Therefore, only a single frame is used for each the pre- and post-sintered images. In order to find the specific frames used for each of the two images, the location of the laser was tracked. By taking the difference between consecutive image frames, the pixel with largest temperature change corresponds to the laser's current location. The selection of the pre- and post-sintered images will be described in the following paragraph.

Different data filtering schemes were used for the even and odd layers of the build because of the alternating scan strategies between layers seen in Figure 9. For the even layers, which had the vertical scan lines, when the laser's location was about to enter a specific column, that corresponding frame was used for the pre-sintered image for that column of three tensile bars. When the laser spot had just exited a specific column, that corresponding frame was used for the

post-sintered image for that column of tensile bars. This same strategy was used for the odd layers but on a row-wise basis instead of column based. A similar strategy was also used for the outline scans, but instead of looking at a row or column, an area surrounding each bar was used to try to get the closest time before and after the laser entered and exited the bar's region in the build surface to get the most accurate temperatures for the outline scan. During this post processing, it was discovered that the heat shield blocked portions of the last row of bars in the first build conducted for this experiment. Therefore, the last of row of bars was unable to be analyzed using the stationary reference camera. The bore-sighted camera however, is not affected by the heat shield locations as the laser has full view of the build surface, and therefore so does the bore-sighted camera.

The stationary reference camera along with the bore-sighed camera, preformed non-uniformity corrections (NUC) intermittently (FLIR Systems, Inc., 2013). This action corrects for the varying responses among the pixels in the camera's sensor. It is an automatic correction that the camera performs for roughly 2 seconds. They cause the entire frame of the camera to saturate at a minimum temperature reading of the camera during the correction process. Due to the intermittent nature of the corrections, they affected the thermal images of random bars in random layers. Therefore, to not cause artificial cold layers or spots due to this random process, for bars that were affected, their individual pixels were replaced with the corresponding pixels of the previous layer so as to not cause sudden changes in the thermal history that would throw off the thermal analysis.

Bore-sighted SC8243 MWIR Camera Analysis

The bore-sighted camera was set up to have a frame rate of 2.24 kHz, with an image size at that frame rate is 64x64 pixels. Each pixel represents an area of around 300x340 microns. As

stated before, this camera is bore-sighted with the laser through a dichroic mirror which allows the camera's image to always be centered about the laser spot. Within each layer, the camera is triggered to start recording with a 'begin lasing' signal from the Cambridge EC1000 control board which controls both the laser power and the galvanometer position. When the camera is triggered, it records for a predetermined number of frames, set at the beginning of the build to be able to record the entire duration of the longest layer, which was around 30 seconds of sintering. Therefore, the amount of frames to be recorded was set at 67,000 frames calculated with the maximum frame rate of the camera.

For the post-sintered image of each bar for this camera, individual scan lines were combined together to form an entire cross section for each bar for every layer of the gage section. In order to get to that point the videos taken with the bore-sighted camera had to undergo pre-processing to determine when the laser was firing and which tensile bar it was sintering at the time. For ease of analysis, the pixel value of the laser spot was taken for the entire length of each layer's video and analyzed. Since the post-sintered temperature was being captured, the pixel location chosen was the one that corresponded to the trailing edge of the laser spot. This location was found in the beginning of the analysis process for each build and used throughout the entire analysis for both builds. It was found through a simple simulation that the maximum pixel value in the image represented the trailing edge of the laser spot as seen in Figure 14. The simulation looked at the temperature of a single point in space on the powder bed as the laser scanned over it as it would do during the scanning process in a build. The laser power, speed, and spot size used were those that were measured or input into the machine during the builds. The temperature of the spot was viewed as a function of relative position of the center of the laser spot. When the trailing of the edge of the laser spot was coincidental to the point, the point achieved its maximum

temperature. Therefore, this pixel was used for the post-sintered image compilation since it was the point immediately following the laser spot.

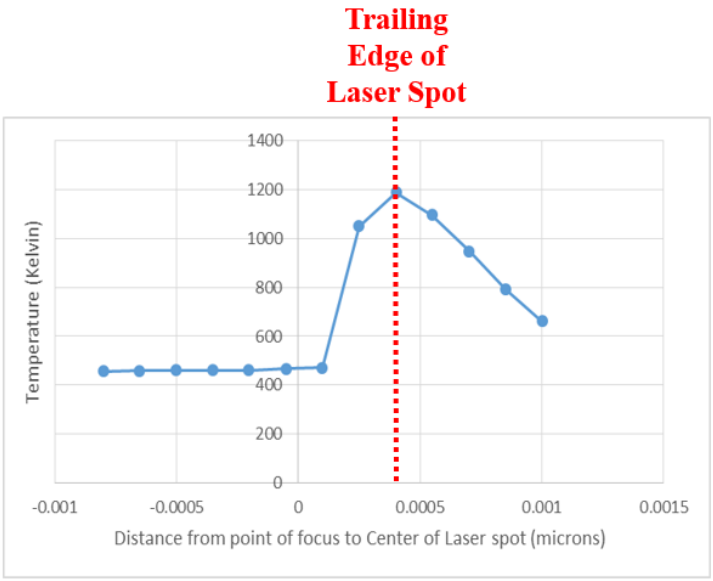

Figure 14: Simulated Thermal Plot Representing Laser Scanning over Powder Bed.

Once the "laser spot" pixel location had been found for all the bore-sighted images, the pixel's temperature over the entire layer was plotted. Examples of each type of layer, vertical and horizontal scanning, can be seen in Figure 15 and Figure 16, respectively.

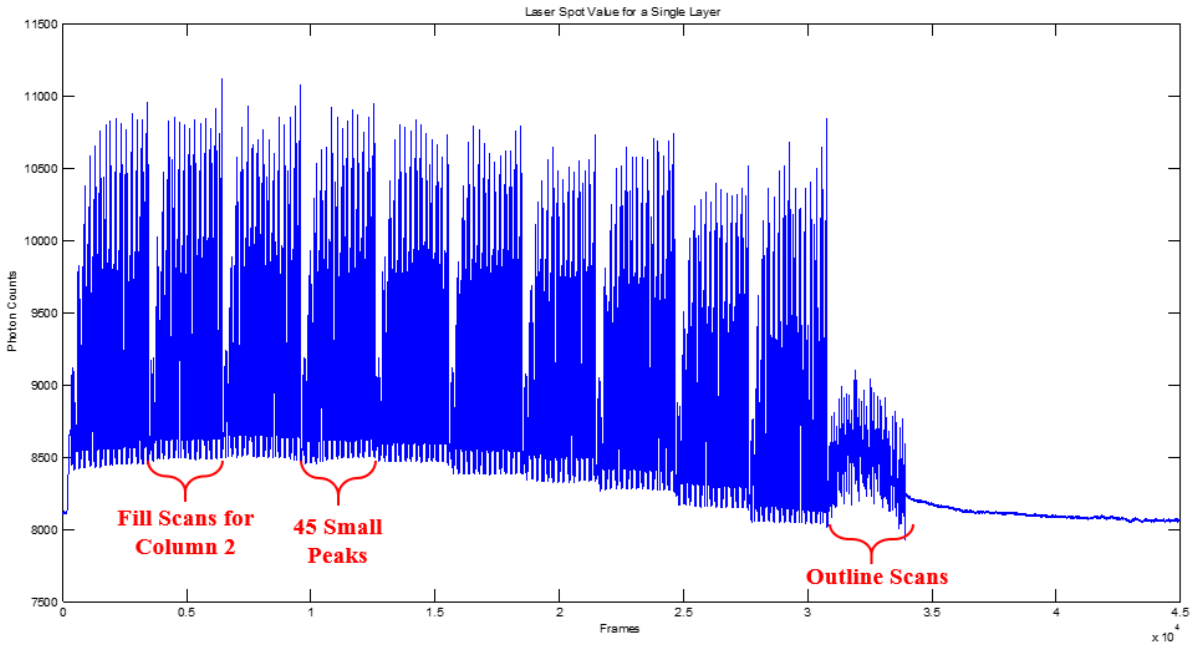

Figure 15: Laser Spot Value during an Entire Layer with Vertical Scan Strategy.

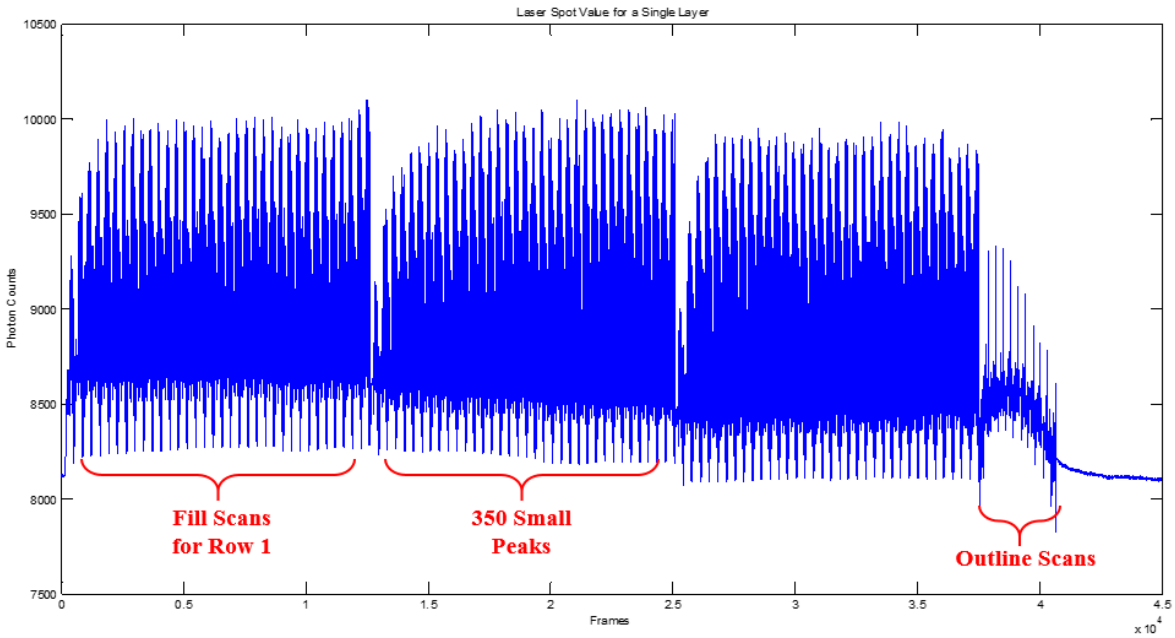

Figure 16: Laser Spot Value during an Entire Layer with Horizontal Scan Strategy.

The larger groups of peaks represent the fill scans of the ten columns or three rows, respectively. Within those large peaks, smaller peaks represented individual scan lines or the

galvanometers passing over an already sintered bar. These peaks were seemingly identical and through timing and temperature value difference, the actual scan lines were found and allocated to their respective tensile bars. For the even layers, each bar had 35 scan lines at a length of about 7 frames. For the odd layers, each bar had 15 scan lines at a length of 15 frames. Therefore, for example, a single column would have a total of 45 scan lines, 15 for each bar, and 45 duplicate false "scan lines" that would appear identical to when the laser was firing but was in fact just the field of view of the galvanometers scanning over where the laser had just fired. As seen in Figure 9, the dotted back lines show the returning motion of the galvanometers from the end of one scan line to the beginning of the next. This motion occurs almost directly over the previously sintered scan line which is still at the elevated temperatures, making it appear almost indistinguishable to when the laser is actually firing. The zoomed in image of one of the large column peaks to demonstrate the identical nature of actual scan lines and false positives can be seen in Figure 17.

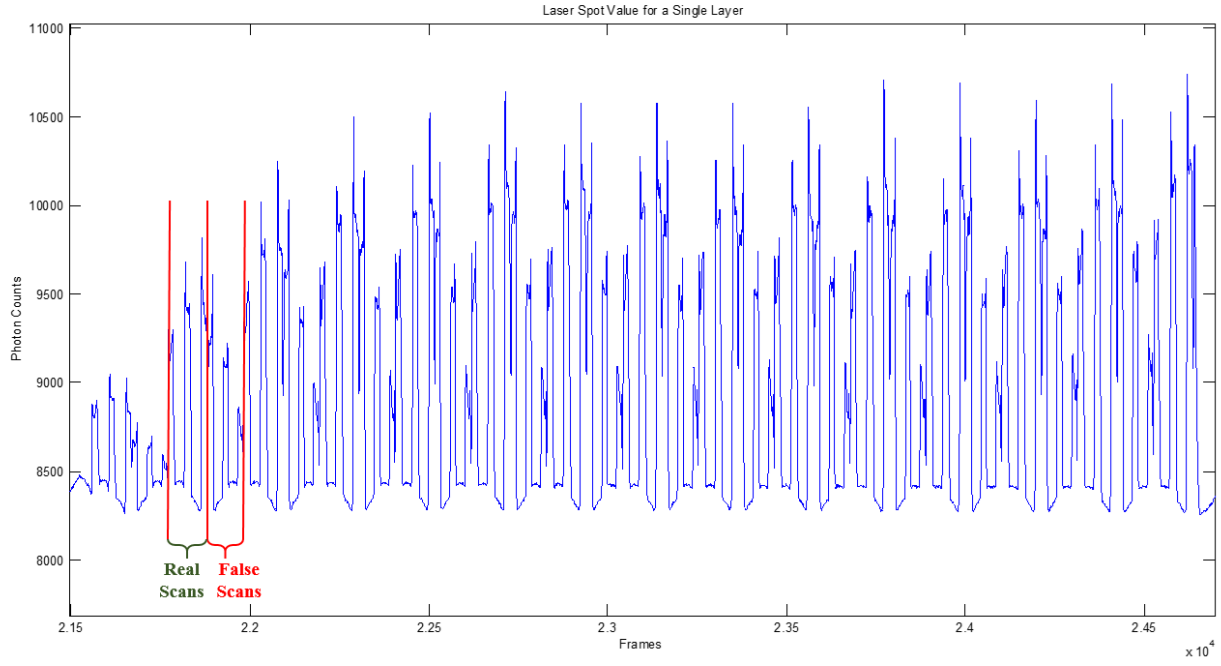

Figure 17: Laser Spot Value for a Single Column of Bars Containing 45 Scan Lines and 45 False Scans.

This difference in number of scan lines was caused by the rectangular cross section of the tensile bars and the laser scan spacing of .274 mm, which produced about 30% of the laser's diameter in overlap. This dimensional mismatch caused severe oscillation when looking at the temperature of all the layers within the gage section. Therefore, the thermal analysis using this camera's data was either filtered using a moving average or each pair of layers, one even and one odd, were averaged together to reduce the noise over the gage section layers.

The pre-sintered image was found by taking the frame of the bore-sighted video before the laser spot entered each tensile bar's cross section before it was sintered, similar to what was performed with the stationary reference camera's images. The image size of the bore-sighted camera was sufficiently large as can be seen in Figure 8 that the entire area of a single tensile bar was able to be measured in a single frame. The pixel values that represented the tensile bar's cross section were saved for each layer in the gage section.

As stated in the section above, the bore-sighted camera also underwent random auto-corrections which caused artificially cold spots for random bars throughout the build. The specific parts of the affected bars were replaced with the corresponding pixels of the layer before so as to not disturb the thermal trend already in place at that time in the build. This action was performed under the assumption that the thermal trends in the build are slow moving and do not see large shifts between two layers.

Chapter 4: Thermal Analysis

The methods discussed below were used to perform the thermal analysis for the data retrieved by both the stationary reference and bore-sighted MWIR cameras. A variety of methods were tried, using correlations between the fracture locations of the tensile specimens and tensile strength with certain calculated thermal signatures as a metric for their utility as a future diagnostic tool. Most of these analysis methods focused on the fill scans or inner area of the tensile bars. This was due to the larger volume of data in that area and the ability to filter out that data for both cameras. All methods described below were implemented for both the pre- and post-sintered images gathered by both MWIR cameras.

The fill analysis methods included the average-fill, cold subregion, hot subregion, thermal range, and stacking cold subregion methods. All these methods used the thermal data from the majority of the area of the tensile bar only excluding the outer region of the bar where the outline scan would occur. This thermal data was gathered before the outline scans occurred for each bar in a given layer so as to only account for the thermal contribution of the fill scan lines.

For the average-fill method, the average of the entire fill region of each tensile bar was taken for each layer of the gage section of the tensile bar. Since the bars were built along the Z axis, the interlayer bond strength is what is being tested, and the hypothesis is that the quality of that bond is directly correlated to the thermal state of the layer. Therefore, taking the average of the entire layer would give an indication of the quality of the layer's bond strength. The layer of minimum and maximum of average temperature were then found and its location compared to the break location of the tensile bar. This method worked well for providing a correlation between thermal history and break location as well as strength and will be further discussed later on.

The cold and hot subregion methods had some of the highest correlations between predicted and actual fracture locations of the tensile bars. In looking at the minimum subregion for each layer, it was believed that this region would correspond to a weak area of bonding between layers caused by under-sintering. The hot subregion behavior was also analyzed, but the method did not have a strong correlation with the mechanical properties and will be discussed further in the results section. Looking at the hot subregion in each layer corresponded with the belief that over-sintering an area can also degrade the bond strength by introducing porosity. However, it is believed that the temperatures of the build did not reach this threshold since the difference between the minimum and maximum subregions in a given layer were less than 1 degree Celsius for the majority of the build. Both methods used a moving window of a predetermined size, be it 3x3, 4x4, or 5x5 pixels of the tensile bar's cross section image, which represented a subregion of the bar's cross section for each layer and took an average of each window. A diagram of the method can be seen in Figure 18.

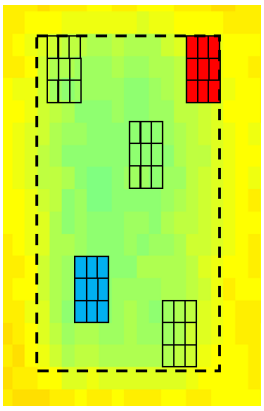

Figure 18: Moving Subregion Method. Pictured is a Single Tensile Bar with 3x3 Pixel Moving Windows with Cold and Hot Subregions Highlighted.

The cold and hot subregions were then found by finding the minimum and maximum of the moving windows for each layer. The cold subregion was then analyzed for all layers of the

gage section for each bar and the minimum of those cold subregions for the entire gage section was then compared to the break location of the corresponding bar.

The thermal range method that was used leveraged the hot and cold subregion average temperatures. It was believed that physically, the largest difference between minimum and maximum temperatures in a given layer would correspond to larger residual stresses within the build which would cause a weak spot for the tensile bar to fracture. The difference was taken between the hottest and coldest spots in a given layer and then plotted for all layers of the gage section. The layer where this value was greatest was found and compared to the break location of the given tensile bar.

The stacking cold subregion method used with the cold subregion was trying to compare where each subregion occurred spatially through all the layers of the gage section for a given bar. This looked at the best subregion size, a 5x5 pixel window, and looked at how much each subregion's location overlapped with the layer next to it. In the procedure, the indices of the location of the subregion for each layer were recorded and then compared to each other. A diagram of how the method was conducted, with the overlap between layers highlighted in white in the diagram, can be found in Figure 19.

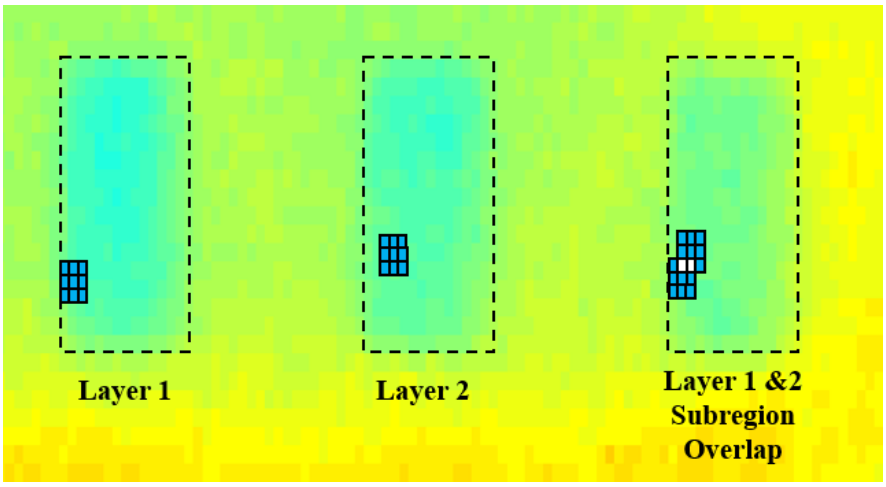

Figure 19: Stacking Cold Subregion Method Diagram.

The number of overlapping pixels between a layer and the one immediately following it were plotted for all layers of the gage section. The largest run of layers that had the most overlap was taken as the possible location for fracture. This method however was unsuccessful since most of the minimum subregions overlapped and no discerning pattern or reason for the break location correlating to a specific behavior of the amount of overlapping could be found.

The outline thermal methods included the average-outline and thermal difference method. The average-outline methods took the whole region just where the outline scan occurred and averaged it, and then compared that value over all layers of the gage section. This was done because it has been found that for failure crack initiation can occur due to surface roughness, which would be dictated by the outline scan. The thermal difference method took the difference between the average temperature of the outline scan and the average temperature of the entire fill area of the tensile bar for a single layer and compared that difference over all the layers in the gage section. This method was not as successful as other methods that were implemented.

Smoothing Techniques

For all the thermal methods used, various smoothing techniques were used to enable visibility of trends, noise reduction, and therefore better predictions of break location. Most of the smoothing consisted of taking a moving average of the data in order to filter the data slightly due to the alternating layer scan strategy. Moving average lengths, also described as windows, ranged from 4 to 20 layers. Better predictions came out of smaller windows. For example, a moving average of 4 for the coldest subregion and average of the entire fill area produced the best break location predictions. From looking at the fracture surfaces of the bars, seen in Figure 20, the fracture locations being initiated within a window of 4 layers are confirmed. Since the fractures are very brittle and the layer stratification causes the cracks to propagate near perpendicular to the loading axis, a small moving average window makes sense.

Figure 20: Examples of Fracture Surfaces for Various Tensile Bars.

Other smoothing techniques that were employed were due to the alternating scan strategy of the build. Since the thermal state of alternating layers would differ as a result of varying number and direction of scan lines, the various thermal methods (average-fill, cold subregion, hot subregion, etc.) were also analyzed by looking at just even or just odd layers. For the stationary reference camera, where the difference between alternating layers was not as significant, this smoothing technique did not offer much improvement versus looking at every layer. For the bore-

sighted camera, comparing only the even or only odd layers reduced a lot of noise when looking at all the layers of the gage section. This was in part due to the dimension mismatch between even and odd layers. This technique of looking at only the odd or only the even layers, however was less successful than other methods in fracture location prediction. It is believed that when a cold region is produced in a single layer, that that region can be 'fixed' by the following layer if there is sufficient thermal energy to counteract the cold area. This phenomena, however, cannot be captured when only looking at just the odd or just the even, because it ignores the thermal trends of layers side by side. Due to the analysis and picking out of data from the bore-sighted camera was more time dependent than spatial, the size and shape of alternating layers differed greatly. Therefore, comparing only the even or only the odd layers of the bore-sighted camera improved the predictive nature of the thermal method that this technique was applied to. While this scheme worked well, the moving average described before was the best smoothing technique as it reduced the noise caused between the alternating layers and smoothed slightly beyond that to produce the best results.

Chapter 5: Results

In this section, the best thermal methods, determined by a strong correlation with strength and fracture location, for each IR camera will be the focus of the discussion. Looking at the overall success rates for all the thermal methods, the stationary reference camera had a better ability to predict break locations than the bore-sighted camera. The difference between the two cameras' abilities will be discussed at the end of this section.

Tensile Test Results

For the first build, the average ultimate tensile strength was 39 MPa, and for the second build, the average ultimate tensile strength was 33 MPa. The plot of stress vs strain for each build can be seen in Figure 21 below.

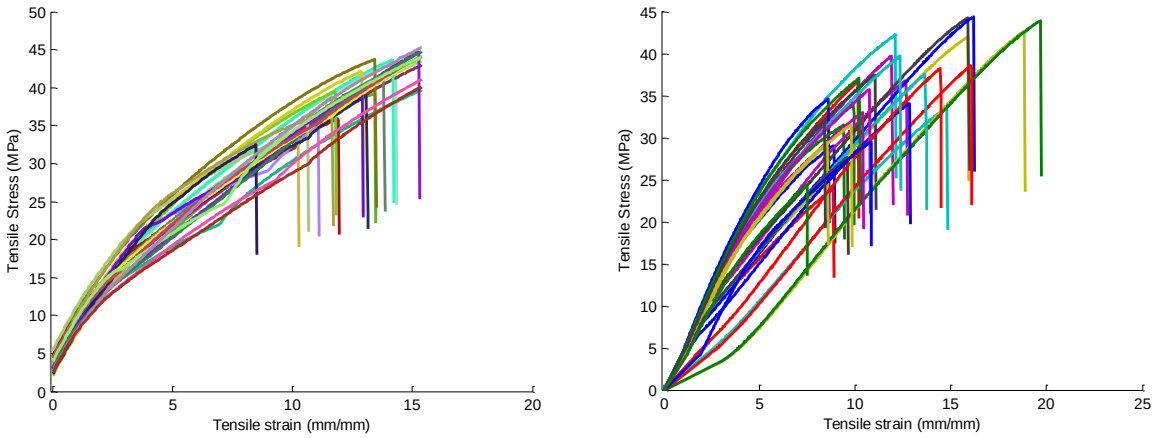

Figure 21: (LEFT) Tensile Results from First Build on 10/11/16 (RIGHT) Tensile Results from Second Build on 11/3/16.

Correlation between thermal methods and mechanical properties

In order to validate the ability of a thermal analysis method to correlate with the fracture location of a tensile bar, that method must first have a high correlation with tensile strength to

prove that that it highlights a weakness in the tensile bar. Using a combination of the thermal and smoothing techniques that are described above, the single temperature value that was used for the predicted failure location was plotted versus the corresponding tensile strength for each tensile specimen. A best fit line was calculated and the fit coefficient was found. These correlation plots were produced for on the best thermal analysis methods for each build. Examples of the minimum subregion temperature for each build can be seen below in Figure 22 and Figure 23.

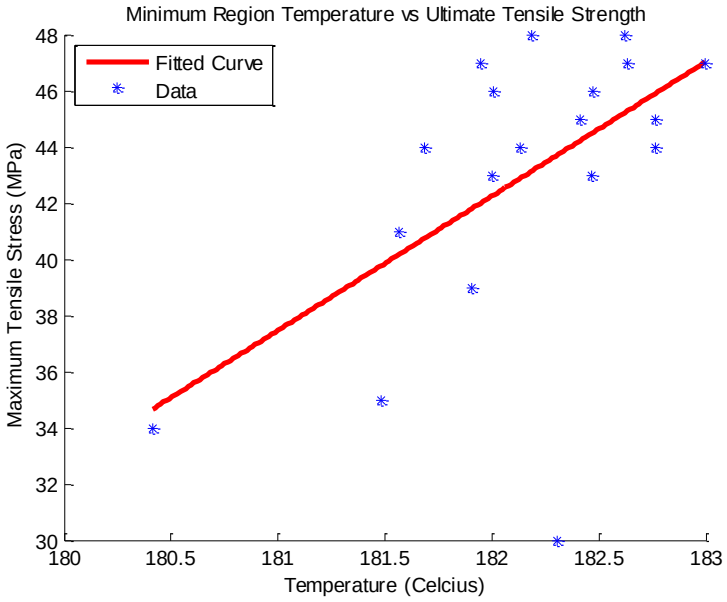

Figure 22: Minimum Temperature Subregion vs Tensile Strength Correlation Plot for 10/11/16 build.

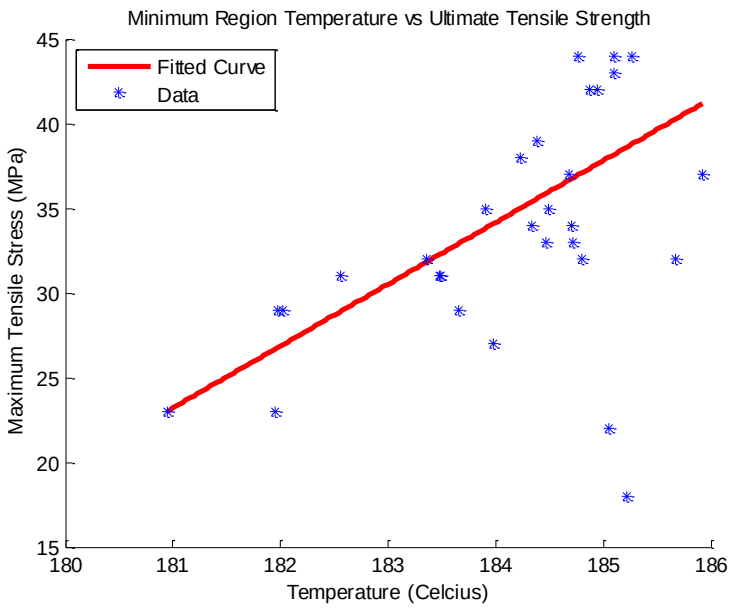

Figure 23: Minimum Temperature Subregion vs Tensile Strength Correlation Plot for 11/3/16 build.

The resultant correlation coefficient for the 10/11 build is .59 and for the 11/3 build is .55. These correlation coefficients were the highest among the methods, so it is expected that this method would be the best predictor of break location for the tensile bars, because better correlation with strength means that the thermal methods is highlighting the weak points in the bar better. Best fits were also created using the same failure temperatures but plotted against the elongation at break of the tensile bars to check the strength of this correlation. Examples of this type of plot can be seen below in Figure 24 and Figure 25. The correlation coefficients for these plots are .24, for the 10/11 build, and .27, for the 11/3 build. Plots for other methods can be found in Appendix A.

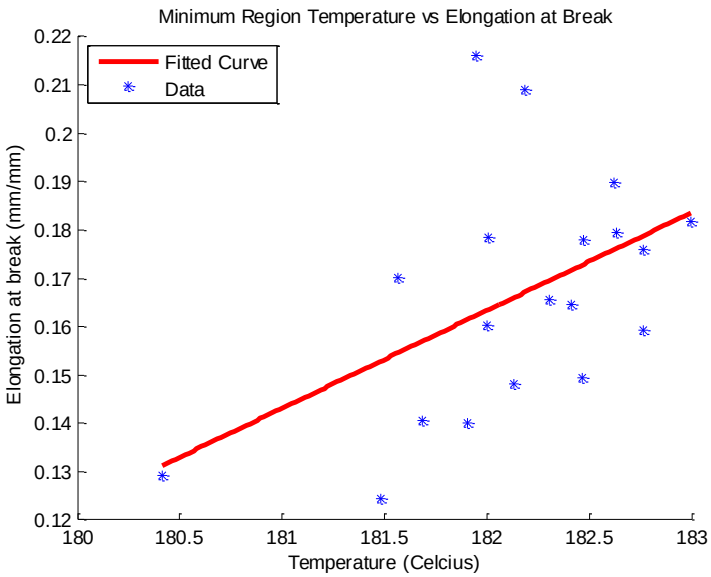

Figure 24: Minimum Temperature Subregion vs Elongation at Break Correlation Plot for 10/11/16 build.

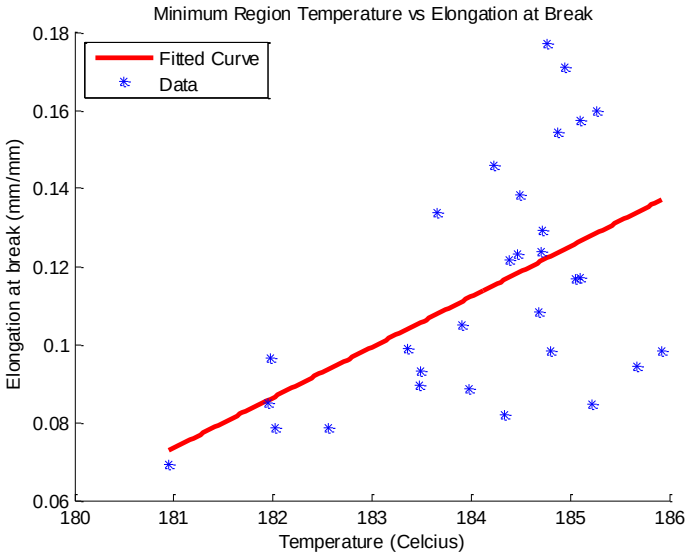

Figure 25: Minimum Temperature Subregion vs Elongation at Break Correlation Plot for 11/3/16 build.

Stationary Reference 6701 MWIR Camera

The best three thermal analysis methods used on the stationary reference camera's images were the minimum subregion, average of the entire layer, and the average temperature of the outline scans. With all the methods, the minimum moving average of 4 layers for each value was

chosen as the possible break location for the tensile bar. The pre-sintered images produced better predictions due to the emissivity changes post-sintering and the time scale of when portions of the bar were lased and the post-sintered image were taken as previously discussed. The success rates for each of these methods for both builds can be found in Table 1 below.

Table 1: Stationary Reference Camera Best 3 Thermal Methods' Results.

Build	Minimum of Coldest Subregion	Minimum of Average of entire layer	Average of Outline Scan
First Build - 10/11/16	45%	45%	35%
Second Build - 11/3/16	77%	70%	80%

All of these methods corresponded to weaknesses in the bonding of the layers and would cause weak areas that would allow cracks to initiate and propagate with greater ease. As seen above in Table 1, the best was the cold subregion, which shows that fracture is dependent on a smaller area than an entire layer. A graph of the best three methods temperature for the gage section can be found in Figure 26. The moving average of 4 layers was implemented to smooth the curves and the absolute minimum layer for each method was found. For the average of the outline scan, the pre-sintered image was taken after the fill scans were completed. It is believed that this method worked well because the image, due to the time when it was taken, was able to record a more accurate picture of the temperature of the outer area of the tensile bar. This pre-sintered outline image took into account some of the influence of sintering since the outline scan overlaps with some portion of the fill area. Results for other thermal methods that were described in the section above but did not perform well can be found in Appendix A.

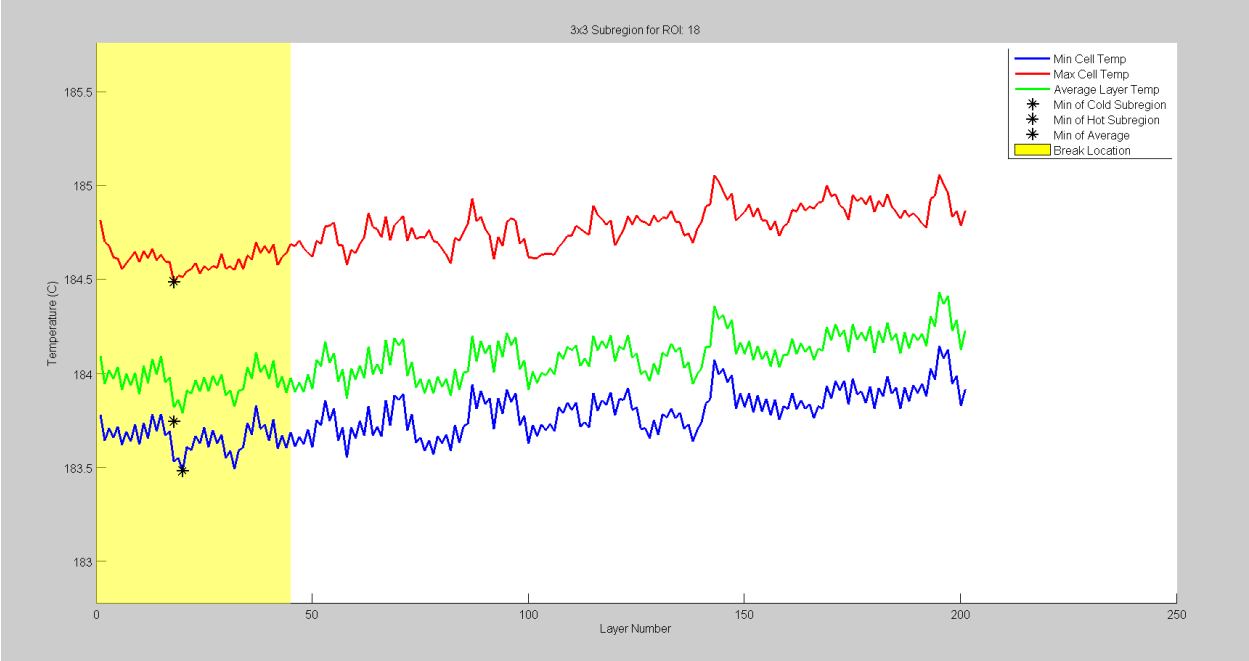

Figure 26: Thermal Plot of Best Three Methods for Gage Section for Tensile Bar 18 in the 11/3/16 Build.

Bore-sighted SC8243 MWIR Camera

For the bore-sighted camera, different thermal methods worked better for different builds. The only difference between the builds that is able to be quantified is that the quartz lamps, that provide fine temperature control on the powder bed, had set points 1 degree Celsius higher during the second build than the first build. For the first build performed on October 11, the best methods were similar to that of the stationary reference camera. The success rates for this build for the bore-sighted camera can be found in Table 2 below.

Table 2: Best Three Thermal Methods for 10/11/16 Build with Bore-sighted Camera Measurements.

	Min of Coldest Subregion	**Min of Average**	**Min of Hottest Subregion**
Build #1 – 10/11/16	43%	43%	43%

The best three methods were finding the minimum of the coldest subregion, average, and hottest subregion of each layer for the tensile bars. An example of the fracture location thermal plots for the gage section for this build can be found in Figure 27 below.

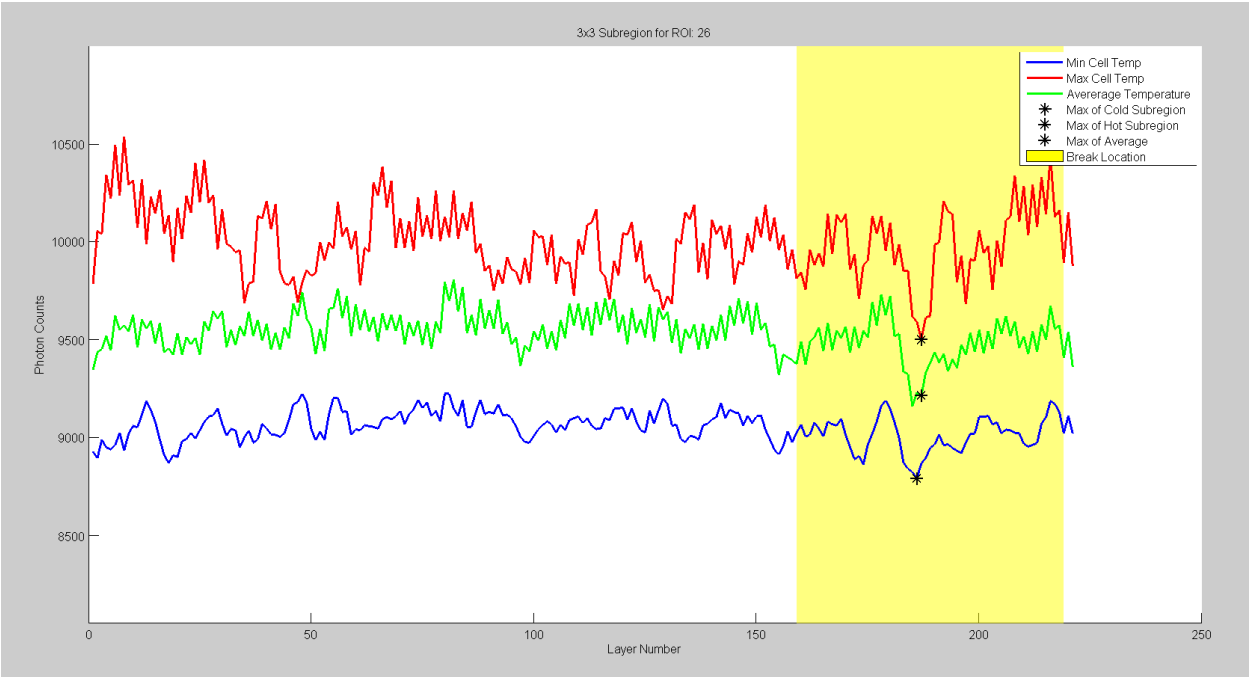

Figure 27: Best Three Thermal Methods for 10/11/16 Build with Bore-Sighted Camera Measurements.

For the second build, performed on November 3, the behavior was reversed. The best three methods were finding the maximum of the cold subregion, average, and hot subregions. The success rates for these methods for the November 3 build can be found in Table 3 below. An example of the fracture location thermal plots for the gage section for this build can be found in Figure 28 below.

Table 3: Best Three Thermal Methods for 11/3/16 Build with Bore-sighted Camera Measurements.

	Max of Coldest Subregion	**Max of Average**	**Max of Hottest Subregion**
Build #2 – 11/3/16	56%	60%	53%

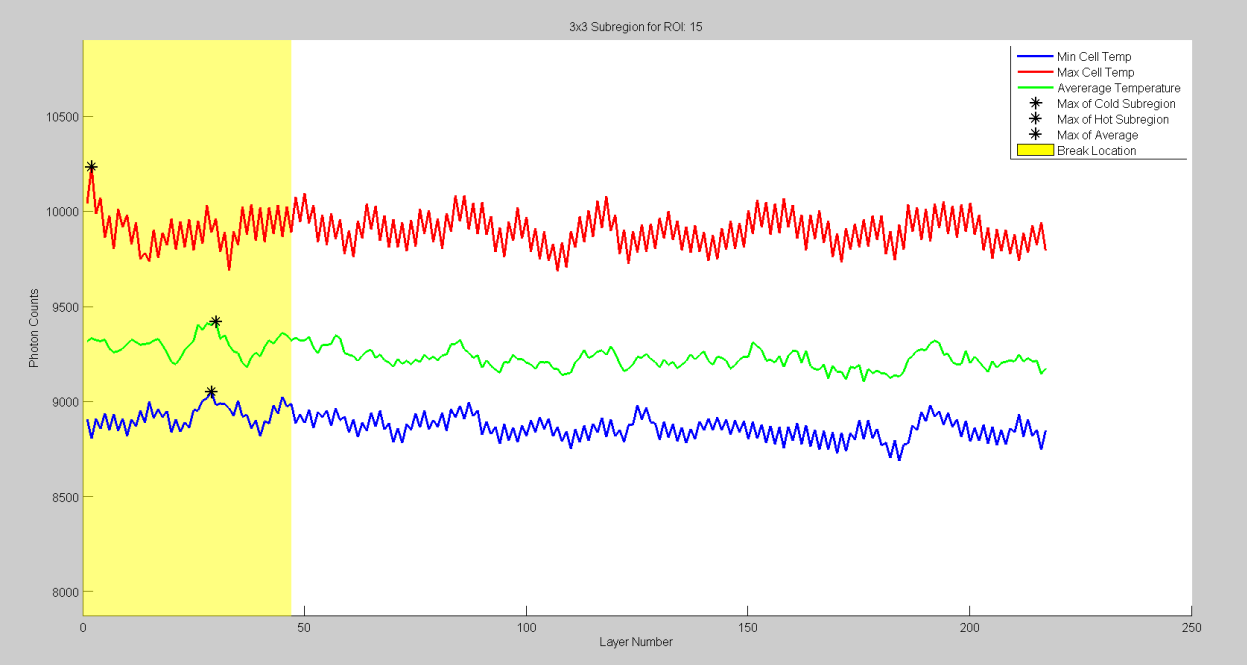

Figure 28: Best Three Thermal Methods for 11/3/16 Build with Bore-Sighted Camera Measurements.

Although the only difference between the two builds was 1 degree on the build surface, the bore-sighted camera's results changed drastically. The physical reasons behind this change can only be speculated on at this time. It is believed that one possible reason for the change of best methods is that off gassing produced while each layer is sintered causes reflections and absorption of infrared light that affect the camera's image of the build surface. This could result in the camera viewing a hotspot while on the same location of the build surface actually exists a cold spot (Benedict, 2017). Results for other thermal methods that were described in the section above but did not perform well can be found in Appendix A.

The overall success rates for the bore-sighted camera independent of build or methods, were significantly lower than that of the stationary reference camera. Both cameras are mid-wave IR cameras that should not be influenced by the laser's wavelength. However, the optical trains that the cameras' line of sight passes through are vastly different. Both camera's line of sight travels through ZnSe windows that allows the infrared light to pass through. That is the only optical

object the stationary reference camera's field of view passes through. However, for the bore-sighted camera, its image is reflected by the galvanometer scanning mirrors and dichroic mirror. The laser is also being reflected on these two surfaces as well as traveling through the same ZnSe window that the bore-sighted camera looks through. All three of these surfaces have the ability to heat up due to either direct absorption of the laser's wavelength by the base material of the optical surface or from possible surface contamination that would absorb the laser's wavelength. This heating up of optics would produce a dynamically changing error for the camera (Milner, 2017). A handheld FLIR E60 long-wave IR camera was used to view the dichroic mirror as the laser scanned the build surface during a single layer. As seen in Figure 29 below, an uneven distribution of the laser's power which can produce variable heating of this optical element is present.

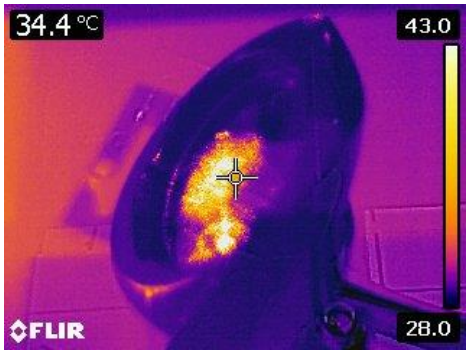

Figure 29: IR Image of Dichroic Mirror during Lasing of Layer.

This heating can change over time and cause the dynamic error that would affect the bore-sighted camera's images. This is the most likely cause of the lower success rates of prediction for the boresight camera as the prediction methods are all relative to each tensile bar instead of a set threshold temperature. If there was a constant error that would produce an offset in the camera, it should not affect the camera's ability to find cold regions within the build surface, but since the possible error sources produce a non-uniform heating of optical elements, the camera's images are spatially affected.

Chapter 6: Conclusion

Looking at all the thermal methods that were used for both MWIR cameras, the most successful method that predicted the break location of the tensile bars was finding the minimum cold subregion for each tensile bar in the gage section. The size of the subregion needed to be large enough to be able to identify a weak spot with enough size to cause that layer to fracture before other. If the subregion was too small, it did not correlate with the fracture location as well. The cold subregion physically corresponds to a weak spot in the interlayer bonding that would give way to fracture when under tensile loading. The best subregion was found to be 5x5 pixels in size, which corresponds to an area roughly 1500x3200 microns or 1.5x3.2 mm.

The correlation between the thermal history and the tensile strength of the bars was not as high as expected, given the high success rates of fracture location prediction. The fracture location prediction may have had a higher correlation between the thermal history and the fracture strength because the testing procedure for the tensile bars is affected by human error in the placement of the tensile bar in the testing jaws. This is suggested since each tensile bar was manually loaded into the tensile jaws, the alignment with the long axis of the tensile bar may have been slightly off from the loading axis of the tensile machine. This could allow the loading to not be exactly perpendicular to the layer stratification, which would allow the tensile strength to not solely depend on the interlayer bond strength, which was the assumption of this study. Another reason for the poorer correlation with tensile strength is that differences in minimum temperature between bars can be as low as tenths of a degree C, which is well within the error range of the cameras which is +/- 2 degrees C (FLIR, 2017).

When viewing the fracture location prediction success rates between the two cameras, it is clear that the optical track of a given camera effects the results significantly. Even though the stationary reference camera only had a frame rate of 30 Hz compared to the bore-sighted camera with its frame rate of 2.24 kHz, it was the more successful camera, which demonstrates that high speed monitoring is not necessary if looking at the overall quality of a layer. It may be needed for more specific monitoring for instance with the melt pool. However, for layer bond strength, an overall image is needed, rather than images of individual scan lines. The pre-sintering image thermal data had a higher correlation with mechanical properties than the post-sintering image thermal data. After sintering occurred, the emissivity of the bar is not consistent, as some portions are still liquid with a lower emissivity than the powder emissivity that is input into the camera, and therefore would affect the measurements. Since measuring the temperature of the bars immediately following sintering is complicated by the variable emissivity, a period of time needs to elapse before measurements can be taken where the emissivity is near constant throughout the tensile bar. In using the either the pre- or post-sintered images, the need for high speed cameras diminishes, as a single image can be used for the pre-sintered image for either camera versus the post-sintered image had to be pieced together from several images with the bore-sighted camera. This allows for a smaller storage of data, which when the need for keeping all data from builds as a quality check, will decline the need for larger storage servers.

Appendix A: Thermal Method Results

Table A1: 5x5 Hot Subregion Smoothed with Moving Average of 4 Layers

Build	Stationary Reference Camera Pre-Sintered	Stationary Reference Camera Post-Sintered	Boresighted Camera Pre-Sintered	Boresighted Camera Post-Sintered
Build #1	25%	20%	10%	43%
Build #2	70%	20%	10%	10%
Overall Success Rate	52%	20%	20%	26%

Table A2: Fill Thermal Range Method – No Smoothing Method Used

Build	Stationary Reference Camera Pre-Sintered	Stationary Reference Camera Post-Sintered	Boresighted Camera Pre-Sintered	Boresighted Camera Post-Sintered
Build #1	40%	30%	17%	23%
Build #2	23%	43%	40%	20%
Overall Success Rate	30%	38%	28%	21%

Table A3: 3x3 Pixel Sized Cold Subregion – Smoothed with 4 Layer Moving Average

Build	Stationary Reference Camera Pre-Sintered	Stationary Reference Camera Post-Sintered	Boresighted Camera Pre-Sintered	Boresighted Camera Post-Sintered
Build #1	40%	15%	17%	43%
Build #2	73%	73%	13%	10%
Overall Success Rate	60%	50%	15%	27%

Table A4: Outline-Fill Thermal Difference Method with No Smoothing Technique

Build	Stationary Reference Camera Pre-Sintered	Stationary Reference Camera Post-Sintered	Boresighted Camera Pre-Sintered	Boresighted Camera Post-Sintered
Build #1	45%	40%	N/A	N/A
Build #2	5%	0%	N/A	N/A
Overall Success Rate	25%	20%	N/A	N/A

Table A5: Average-Fill Method with No Smoothing Technique Used

Build	Stationary Reference Camera Pre-Sintered	Stationary Reference Camera Post-Sintered	Boresighted Camera Pre-Sintered	Boresighted Camera Post-Sintered
Build #1	40%	40%	17%	43%
Build #2	16%	16%	7%	10%
Overall Success Rate	28%	28%	12%	27%

References

Austin, U. o. (2012, December 6). *Selective Laser Sintering, Birth of an Industry*. Retrieved 2017, from The Univeristy of Texas at Austin Mechanical Engineering: http://www.me.utexas.edu/news/news/selective-laser-sintering-birth-of-an-industry

Benedict, M. (2017, February 22). Senior Materials Engineer, Materials & Manufacturing Directorate, AFRL.

Bourell, D. L., Watt, T. J., Leigh, D. K., & Fulcher, B. (2014). Performance Limitations in Polymer Laser Sintering. *Physics Procedia*, 147-156.

Buls, S., Clijsters, S., & Kruth, J.-P. (2014). Homogenizing the melt pool intensity distribution in the SLM process through system identification and feedback control. *Solid Freeform Fabrication Symposium*, (pp. 6-11). Austin, TX.

Edmund Optics Inc. (2017). *EO-1312M ½" CMOS Monochrome USB Camera* . Retrieved from Edmund Optics: https://www.edmundoptics.com/cameras/usb-cameras/eo-usb-2-0-cmos-machine-vision-cameras/59365/

FLIR. (2017). *FLIR A325sc Infrared Camera Datasheet.* Retrieved from FLIR Research & Science: http://www.flir.com/science/display/?id=46623

FLIR. (2017). *FLIR A6700sc MWIR Datasheet.* Retrieved from FLIR Research & Science: http://www.flir.com/science/display/?id=67022

FLIR Systems, Inc. (2013). *SC8240 User's Manual.* Nashua, NH, USA: FLIR Systems, Inc.

Krauss, H., Eschey, C., & Zaeh, M. F. (2012). Thermography for Monitoring the Selective Laser Melting Process. *Solid Freeform Fabrication Symposium*, (pp. 999-1014). Austin, TX.

Milner, D. T. (2017, February 16). Dynamic Erros in Infrared Optics. (S. Taylor, Interviewer)

Optotherm Thermal Imaging. (2017). *Camera Components Infrasight IS640 Radiometric Infrared Camera Competitive Advantages*. Retrieved from Optotherm: http://www.optotherm.com/camera-advantages.htm

Phillips, T., McElroy, A., Fish, S., & Beaman, J. (2016). In-Situ Laser Control Method for Polymer Selective Laser Sintering (SLS). *Solid Freeform Fabrication Symposium*, (pp. 1381-1396). Austin, TX.

SPI Lasers Limited. (2015). Retrieved from http://www.spilasers.com/application-additive-manufacturing/selective-laser-sintering-and-melting/

Wroe, W. W. (2015, August 2015). *Improvements and effects of thermal history on mechanical properties for polymer selective laser sintering (SLS).* Retrieved from The Univeristy of Texas at Austin Texas ScholarWorks: https://repositories.lib.utexas.edu/handle/2152/31997?show=full

Wroe, W. W. (2015). *Improvements and Effects of Thermal History on Mechanical Properties for Polymer Selective Laser Sintering (SLS).* Austin: University of Texas, Austin.